Exploring laser-induced damage threshold in metallic coatings across a fifteen-order-of-magnitude-range of pulse lengths

Erikas Atkočaitis, Marco Jupé, Urtė Kimbaraitė, Laurent Gallais, Emilija Žutautaitė, Kevin Kiedrowski, Morten Steinecke, Lars Herrero, Mindaugas Ščiuka, Arūnas Varanavičius, et al.

Research Article | Vol. 33, No. 21 / 20 Oct 2025 / Optics Express 44843
Optics EXPRESS

Exploring laser-induced damage threshold in metallic coatings across a fifteen-order-of-magnitude-range of pulse lengths

ERIKAS ATKOČAITIS,[1] MARCO JUPÉ,[2] URTĖ KIMBARAITĖ,[1,3] LAURENT GALLAIS,[4] EMILIJA ŽUTAUTAITĖ,[1] KEVIN KIEDROWSKI,[2] MORTEN STEINECKE,[2] LARS HERRERO,[2] MINDAUGAS ŠČIUKA,[3] ARŪNAS VARANAVIČIUS,[1] GAUDENIS JANSONAS,[1] AND ANDRIUS MELNINKAITIS[1,*]

[1]*Laser Research Center at Faculty of Physics, Vilnius University, Saulėtekio al. 10, LT-10223 Vilnius, Lithuania*
[2]*Laser Zentrum Hannover e.V., Hollerithallee 8, 30419 Hannover, Germany*
[3]*UAB Lidaris, Saulėtekio al. 10, LT-10223 Vilnius, Lithuania*
[4]*Aix Marseille Univ, CNRS, Centrale Med, Institut Fresnel, Marseille, France*
[*]*andrius.melninkaitis@ff.vu.lt*

Abstract: We investigated the laser-induced damage threshold (LIDT) of seven metallic (Ag, Al, Au, Cr, Ta, Ti, W) and two semiconductor (Si, Ge) coatings on glass substrates as a function of the laser pulse duration using 1-on-1 and S(1000)-on-1 testing. Experiments spanning pulse durations from 10 femtoseconds to 10 seconds revealed two distinct LIDT scaling laws for pulsed and continuous-wave (CW) regimes. Numerical simulations of laser radiation coupling and heat diffusion in gold coating explained the observed scaling. They predicted the transition between pulsed and CW regimes, which depends on film thickness and material properties. For short pulses, LIDT is dominated by the metallic film, while for long pulses, heat dissipation into the substrate becomes critical. These findings enhance the understanding of LIDT scaling and the thermal dynamics of metallic coatings.

1. Introduction

Metallic coatings played a crucial role in the development of the first laser, where silver-coated mirrors provided the necessary reflectivity to amplify light within a ruby rod [1]. However, the high absorptance of metallic coatings led to a relatively low laser-induced damage threshold (LIDT) compared to that of dielectric coatings, which limited the power scaling capabilities. As a result, metallic coatings have been used primarily in low-power imaging [2], spectral analysis [3,4], and sensor applications due to their broadband reflectivity, cost-effectiveness, and surface plasmon resonance properties [5]. Except for gold coatings on polished copper optics in CO_2 lasers, metallic mirrors have been largely replaced by dielectric multilayer coatings in high-power laser systems.

The LIDT of metallic coatings has been a subject of investigation since the invention of the laser. Sparks et al. [6] examined copper and aluminum films with 100 ns pulses and gold and silver films with 150 ps pulses, showing that the LIDT depends on various parameters such as pulse length, pulse shape, number of pulses, and optical properties (e.g., absorption and reflectivity). While for dielectrics, with intensities close to the damage threshold, multiphoton and avalanche ionization are the driving mechanisms for laser radiation coupling in the material [7]. For metals, photon energy is transferred to free electrons via the inverse bremsstrahlung

#563537 https://doi.org/10.1364/OE.563537
Journal © 2025 Received 26 Mar 2025; revised 25 May 2025; accepted 10 Jul 2025; published 15 Oct 2025

Optics EXPRESS

process, increasing their kinetic energy through electron-phonon interactions. The kinetic energy is then transferred from the electrons to the lattice, and a thermal equilibrium is achieved between the electrons and the lattice. As irradiation continues, a series of thermal processes occur that ultimately result in macroscopic damage to the material [6–13]. These thermal mechanisms play a crucial role in the determination of the LIDT of metallic coatings, particularly under long-pulse and CW irradiation conditions. Furthermore, LIDT was found to be linearly dependent on coating thickness up to the optical penetration depth, after which the threshold approaches the bulk material damage threshold, particularly for pulses ranging from 200 fs to 10 ps [14,15]. Under the conditions investigated, the effect of coating thickness on LIDT became minimal for coatings thicker than 50 – 500 nm, depending on the material being studied.

In recent years, metallic and hybrid metal-dielectric coatings have regained interest due to their importance in femtosecond laser technology. Their ability to reflect broadband pulses over a wide range of angles of incidence (AOI) with low dispersion has made them particularly relevant in ultrashort laser optics [16–18]. However, the LIDT of metallic coatings remains a key challenge, particularly under varying pulse durations. A deeper understanding of LIDT scaling laws is essential for improving optical component reliability in high-power laser systems, guiding material selection, and mitigating failure risks in industrial and scientific applications.

To better understand the behavior of LIDT, various theoretical models have been developed. One of the first approaches is a one-dimensional heat flow calculation model described by Wood [8], where a semi-infinite medium (without coating) is assumed with temperature-independent absorption properties. While being just a first-order approximation, the model predicts that LIDT scaling for thermal damage is governed by the balance between the deposited power and the dissipated power in the CW regime and the thermal capacity of the exposed area for pulses shorter than the heat diffusion time.

The LIDT scaling with pulse duration is also important for micro- and macro-machining [19,20]. Ablation studies have partially confirmed the predictions by Wood, showing that in the 500 fs – 10 ps range, the ablation threshold exhibits only a weak dependence on pulse duration for materials such as copper and silicon [21]. Similar trends were observed for aluminum, copper, nickel and tungsten in the 15 – 100 fs regime [22], although scaling laws were not explicitly stated in some studies [23,24]. In contrast, Hashida et al. [25] showed that in the 70 fs – 5 ps range, the ablation threshold scales with the pulse duration as $\tau^{0.25-0.67}$, depending on the ablation depth. Stuart et al. [7] also found that the LIDT of gold coatings follows a $\tau^{0.5}$ dependence in the 200 ps – 1 ns range, while remaining pulse duration-independent in the 100 fs – 200 ps range. Y. Zhu et al. [26] recently reported opposite dependence in SiO_2-coated aluminum mirrors at 1030 nm wavelength, with pulse widths ranging from 200 fs to 11 ps, indicating that the LIDT deviates from the square root scaling law ($\tau^{-0.063}$) as the pulse width decreases below 10 ps.

Although previous research has focused primarily on short pulses and a limited set of metallic materials, data on the LIDT dependence under CW irradiation remain particularly scarce and underexplored. Furthermore, a clear consensus on the influence of material properties on LIDT has yet to emerge, as various studies report conflicting and mutually inconsistent results. These inconsistencies highlight the need for a more comprehensive understanding of LIDT. Despite these challenges, recent attention to LIDT scaling with pulse duration under CW irradiation conditions also requires experimental validation of existing models to provide reliable LIDT scaling predictions. Given these gaps, it is essential to conduct a systematic investigation of the LIDT scaling across a wide range of pulse durations.

This study aims to address the gaps by systematically studying LIDT across pulse durations from fs to CW on widely used metallic coatings. Specifically, we conducted an experimental study on seven metallic coatings (aluminum, gold, silver, tantalum, titanium, tungsten, and chromium) and two semiconductor coatings (silicon and germanium) for pulse durations ranging from 10 fs to 10 s. LIDT measurements are performed according to ISO standards [27] using the

Optics EXPRESS

1-on-1 and S(1000)-on-1 protocols in the near-infrared spectral range (1030 nm, 1064 nm, 1070 nm).

2. Experimental methods

2.1. Sample preparation and characterization

All experimental coatings were deposited at the Laser Zentrum Hannover (LZH, Germany) using a Denton Desktop Pro sputtering system equipped with two magnetrons. Nine Borofloat glass substrates (60 mm in diameter) were coated with metallic and semiconductor layers of varying thicknesses (see Table 1). Before coating, the substrates were cleaned using an ultrasonic cleaning system, with no additional plasma vapor treatment applied. The metal layers were deposited via DC magnetron sputtering (sputtering current: 600 mA), while the dielectric layers were deposited via RF magnetron sputtering (RF power: 144 mW). The typical metallic coating structure is shown in Fig. 1. In most cases, the structure consists of a substrate, two adhesive layers (Al_2O_3 and Al), followed by the main coating material. Adhesive layers were necessary for most coatings (except Ge, Si, and Ti) to prevent substrate delamination. In addition, a protective layer of SiO_2 was applied to the Ag, Al, Ta, and Ti coatings to prevent oxidation. Because the overcoat is transparent to the wavelength of investigation, its effect on LIDT is assumed to be negligible. The coatings were analyzed for reflectivity at the investigated wavelength (see Table 2), while thickness measurements were made by analyzing cross-sections prepared using focused ion beam (FIB) milling and examined with a scanning electron microscope (Helios NanoLab 650).

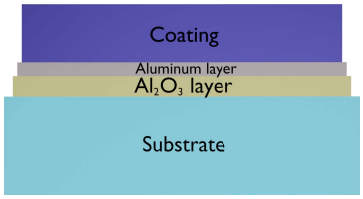

Fig. 1. The general structure of the coatings. The adhesive layer and protective layer (not shown) are not applied for all coatings, see more in Table 1.

Table 1. List of material coatings and their parameters.

Topmost coating material	Adhesive layer	Protective layer	Deposition method	Deposition rate (nm/min)	Metallic layer thickness (nm)
Ag	Al_2O_3 + Al	SiO_2	DC	3.5	45
Al	Al_2O_3 + Al	SiO_2	RF	3.2	271
Au	Al_2O_3 + Al	-	DC	1	292
Cr	Al_2O_3 + Al	-	DC	8.4	198
Ge	-	-	DC	5	1775
Si	-	-	RF	5	1774
Ta	Al_2O_3 + Al	SiO_2	DC	2.8	686
Ti	-	SiO_2	DC	2.5	296
W	Al_2O_3 + Al	-	DC	5.05	234

Before damage testing, the reflectivity R of every sample was characterized by measuring the ratio of reflected and incident light power at 1064 nm wavelengths at ~2 AOI. Later, R was used to deduce absorptance A and was used for numerical simulations.

Optics EXPRESS

Table 2. Material properties. Reflection coefficient (measured in this work), specific heat capacity and melting point are gathered from various literature sources [8,28,29].

Coating material	Reflection coefficient (%)	Specific heat capacity (J/kgK)	Melting point (°C)
Ag	95.11	900	962
Al	88.22	520	660
Au	96.4	450	1064
Cr	33.95	710	1907
Ge	42.32	140	938
Si	32.95	130	1410
Ta	44.93	129	3020
Ti	34.08	235	1725
W	59.24	320	3522

2.2. Measurements of laser damage threshold

LIDT measurements were performed using 1 on-1 and S(1000)-on-1 test protocols, following the ISO 21254-2 international standard [27]. For CW measurements, only the 1-on-1 method was applied. A new test site matrix (of at least 400 test sites) was used for each fixed pulse width. To avoid overlap, the test sites were separated by at least three beam diameters. To ensure the comparability of LIDT data across the full range of pulse durations, irradiation conditions were carefully controlled despite the use of three different laser systems. Beam diameters remained within 195 – 230 μm at the $1/e^2$ level for all measurements except at 10 fs, where a smaller beam diameter of ~100 μm was used. Nevertheless, the LIDT values obtained at 10 fs aligned with the overall trend (see Sec. 4), indicating negligible beam size influence. Beam quality, while not explicitly quantified, showed no deviation from diffraction-limited performance in recorded profiles, and therefore no systematic impact on the LIDT measurements was expected. Measurements for pulse durations between 10 fs and 9 ns were performed at normal AOI with a laser repetition rate of 100 Hz. In the CW regime, an AOI of 10 degrees was used to prevent back-reflection damage to the laser power fiber.

For all pulsed laser tests, incident fluence was controlled using a motorized attenuator. The fluence was kept constant for at least 10 test sites before increasing in steps of no more than 20% of the previous level. Additional levels of irradiation and test sites near the threshold were exposed to refine the determination of LIDT and minimize error bars. The damage exhibited a deterministic pattern across all pulse durations, characterized by a sharp transition in damage probability. Consequently, LIDT values were determined using the highest-before-first-damage (HBFD) method, which is the average of the lowest damaging – and the highest below damage fluence levels. In the CW regime, LIDT was defined exclusively for the 1-on-1 case, as S(1000)-on-1 measurements were not feasible due to temporal overlap with long pulses.

Since the scaling experiments required a wide range of pulse durations, three pulsed laser systems at the Laser Research Center (Faculty of Physics, Vilnius University, Lithuania) and one CW system at Lidaris (Lithuania) were used for LIDT testing. The principal layouts of the LIDT test systems are shown in Fig. 2.

For the pulsed laser LIDT tests (Fig. 2(A))), the beam passed through a wedge (W), partially reflecting to a photodiode (D) for pulse energy monitoring. The transmitted light was attenuated before reaching a second photodiode or power meter (PW) for calibration. A half-wave plate ($\lambda/2$) adjusted polarization before the beam was focused onto the sample (S) using a lens (L). A scattering diode (SD) detected back-scattered light upon damage.

Optics EXPRESS

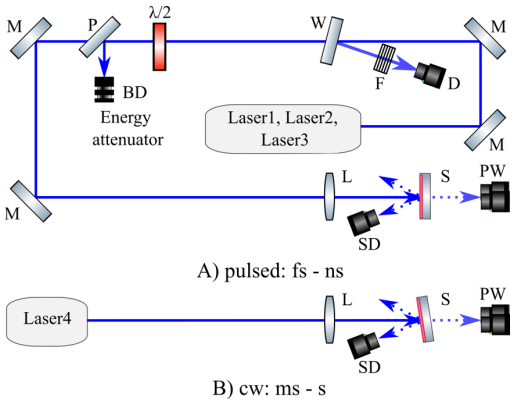

Fig. 2. LIDT measurement setups. (A) represents pulsed laser setups, while (B) represents the CW laser setup. Components: M – guiding mirrors, W – wedge, F – filters, D – photodiode, PW – power meter, $\lambda/2$ – half-wave plate, P – polarizer, L – lens, S – sample, BD – beam dumps, SD – diode for back-scattered light detection.

For 10 fs measurements, the NAGLIS OPCPA [30,31] (similar to the reported in Ref. [32]) system was used, featuring four non-collinear femtosecond and picosecond parametric amplifiers, pumped by Yb:KGW and Nd:YAG lasers. Seed pulses from a femtosecond continuum generator were stretched to ~35 ps before amplification and compressed to 9.5 – 10 fs using SF-57 glass block, fused silica and chirped mirrors.

For pulse durations of 200 fs – 10 ps, a Yb:KGW laser (Light Conversion, Lithuania) at 1030 nm was used, with pulse duration adjusted via an internal compressor. A single longitudinal mode injection-seeded Nd:YAG laser (Innolas, Germany) at 1064 nm was employed for 9 ns measurements.

For CW regime tests (1 ms – 10 s), a Yb-doped glass fiber laser (IPG Photonics, Germany) at 1070 nm was used, with controlled output power and pulse duration. The sample was positioned outside the fiber imaging plane to ensure a near-Gaussian beam profile. In CW LIDT tests (Fig. 2(B))), the laser maintained uniform exposure by controlling power and pulse length.

3. Methodology of thermal modeling

In this section, we present a models used to analyze the LIDT of metallic coatings across the investigated pulse duration range. Although the physical mechanisms causing material damage may be more complex in general, the approach we used remains effective for derived scaling laws, such as the dependence on pulse duration under experimental conditions [7].

Specifically, we employed a thermal model to calculate the temperature distribution within the coating stack and determine the theoretical LIDT by comparing it to a simple criterion, such as the melting point of the metal. More details on the empirical models used are provided in Refs. [8,33], and [34].

To illustrate this approach, we chose to focus on the gold and silver films as a use case, given their well-documented properties [8]. However, similar principles can be applied to other metals using the appropriate material parameters. The parameters used in the simulations, along with the corresponding references, are provided in Table 3.

Optics EXPRESS

Table 3. Model parameters for gold and silver coatings on a fused silica substrate [8,35].

Material	Gold	Silver	Fused silica
Refractive index	0.08-4.6i	0.27-8.7i	-
Specific heat capacity (J/(Kg K))	130	235	830
Density (kg/m^{-3})	19400	10500	2200
Thermal conductivity (W/(m K)	-	-	1.2
Lattice thermal conductivity (W/(m K))	320	430	-
Lattice volumetric heat capacity (J/m^3 K)	2.5×10^6	2.5×10^6	-
Thermal diffusivity (m^2/s)	1.28×10^{-4}	1.72×10^{-4}	6.57×10^{-7}
Melting point (K)	1350	1235	-
Electron heat capacity (J/m^3 K)	$67.6 \times T_e \leq 2000$ K	$63.3 \times T_e \leq 4000$ K	-
Electron-phonon coupling coefficient	2.5×10^{16} for $T_e \leq 3000$ K	1.5×10^{16} for $T_e \leq 5000$ K	-
Electron thermal conductivity	$K_e = \frac{\nu_F^2 C_e(T_e)}{3BT_l + AT_e^2}$, $A = 1.2 \times 10^7$ K^{-2}s^{-1}, $B = 1.23 \times 10^{11}$ K^{-2}s^{-1}	$K_e = K_l \frac{T_e}{T_l}$	-

3.1. Heat-flow model

For CW irradiation, thermal diffusion must be accounted for, and the temperature rise in the stationary regime at the surface may be approximated by the equation [8]:

$$\Delta T = \frac{PA}{2\rho C r \pi D}, \tag{1}$$

where ΔT is the temperature difference between T_{melt} melting point and T_{init} initial temperature, P is incident power, A is absorptance, ρ is the volumetric density, C is specific heat capacity, D is the diffusivity, r is the beam radius. This means that the temperature rise of homogeneous material scales with the linear power density (expressed in W/cm). When converted to fluence ($F = P\tau/\pi r^2$), where τ is pulse width, the LIDT can be expressed as:

$$F = \frac{2\rho C D \tau (T_{\text{melt}} - T_{\text{init}})}{Ar}. \tag{2}$$

Note that threshold fluence becomes directly proportional to pulse duration and inversely proportional to beam radius and absorptance. In the pulsed regime, energy deposition is instantaneous, and thus heat conduction is negligible, leading to the temperature rise:

$$\Delta T = \frac{P\tau A}{\rho C V}, \tag{3}$$

where $V = \pi r^2 h$ is the irradiated volume, h is the thickness of the material. When melting is used as a damage criterion, Eq. (3) can be rewritten for threshold fluence, substituting power for energy ($E = Pt$):

$$F = \frac{T_{\text{melt}} - T_{\text{init}}}{\rho C h A}. \tag{4}$$

Consequently, the LIDT (expressed in J/cm^2) becomes constant in the pulsed regime, independent of the pulse duration or beam radius for pulses shorter than the thermal decay constant. Similar models can be found in the literature; however, these models apply to single-shot irradiation conditions, where linear absorption dominates and no optical fatigue or heat accumulation effects from repetitive pulses are expected. For shorter pulses, electrons and lattices experience nonstationary processes, and thus more sophisticated models are needed [36].

Optics EXPRESS

3.2. Two-temperature model

We have used the Two-Temperature Model (TTM) [36] to describe the thermal response of metallic layers to laser excitation. This model describes the energy transfer inside a metal by applying coupled heat conduction equations for the temperatures of the electrons T_e and the lattice T_l.

$$C_e \frac{\partial T_e}{\partial t} = \nabla(K_e \nabla T_e) - g(T_e - T_l) + S(z,t), \tag{5}$$

$$C_l \frac{\partial T_l}{\partial t} = \nabla(K_l \nabla T_l) + g(T_e - T_l), \tag{6}$$

where C_e and C_l are the electron and lattice heat capacities (J/m^{3}K), K_e and K_l are the corresponding thermal conductivities (W/mK), g (W/m^{3}K) is the electron-phonon coupling coefficient, and $S(z,t)$ is the heat source term due to laser absorption. The laser absorption follows the Beer-Lambert law:

$$S(z,t) = \alpha A I(t) e^{-\alpha z}. \tag{7}$$

This is justified by the fact that the thickness of the metallic films is larger than the optical absorption depth. In this expression, A is the absorptance, $I(t)$ is the laser intensity as a function of time (Wm^{-2}) and α is the absorption coefficient (m^{-1}). In the following simulations, we will consider a pulse of constant intensity during the pulse width. The material parameters in Eqs. (5) and (6), heat capacities and thermal conductivities, depend on both the electron and lattice temperatures. Although there is no necessity to use the TTM for pulses longer than the characteristic exchange time between the electron and lattice subsystems, as the electron and lattice temperatures reach equilibrium, we have applied the same model across the entire range of pulse durations explored in this work for consistency in the absolute values. The model continues to yield valid results, even for longer durations.

3.3. Finite element method-based numerical modeling

To accurately simulate the thermal response of multilayer structures under focused laser irradiation, we employ the Finite Element Method (FEM) in COMSOL Multiphysics (6.3 version). The model accounts for both the multilayer composition and the spatial intensity distribution of the laser beam. The numerical setup is based on an axisymmetric geometry with a Gaussian beam profile (100 µm waist).

Thermal insulation is used as a boundary condition since the component is sufficiently large compared to the heat-affected area during the simulation time. For each pulse duration, ranging from 100 fs to 100 ms, the pulse energy is incrementally increased in discrete steps until the surface temperature reaches the melting point (1350 K for gold and 1235 K for silver), thereby defining the damage threshold. For short pulses (< 9 ns), the onset of damage occurs after the pulse. The material properties, including thermal conductivity and specific heat, are considered temperature-dependent to ensure accurate thermal response modeling.

4. Results and discussion

4.1. Damage Morphology

To analyze the experimental data, let us first take a look at the 1-on-1 damage initiation morphology, which provides crucial insights into the laser-induced damage mechanisms in different pulse regimes. Following ISO procedure, any permanent and apparent changes are classified as "damages". Images of interrogated sites are taken before and after laser irradiation using a differential interference contrast (DIC) Nomarski microscope. Figure 4 presents a compilation of damage morphologies observed across the investigated pulse-length range. As expected

Optics EXPRESS

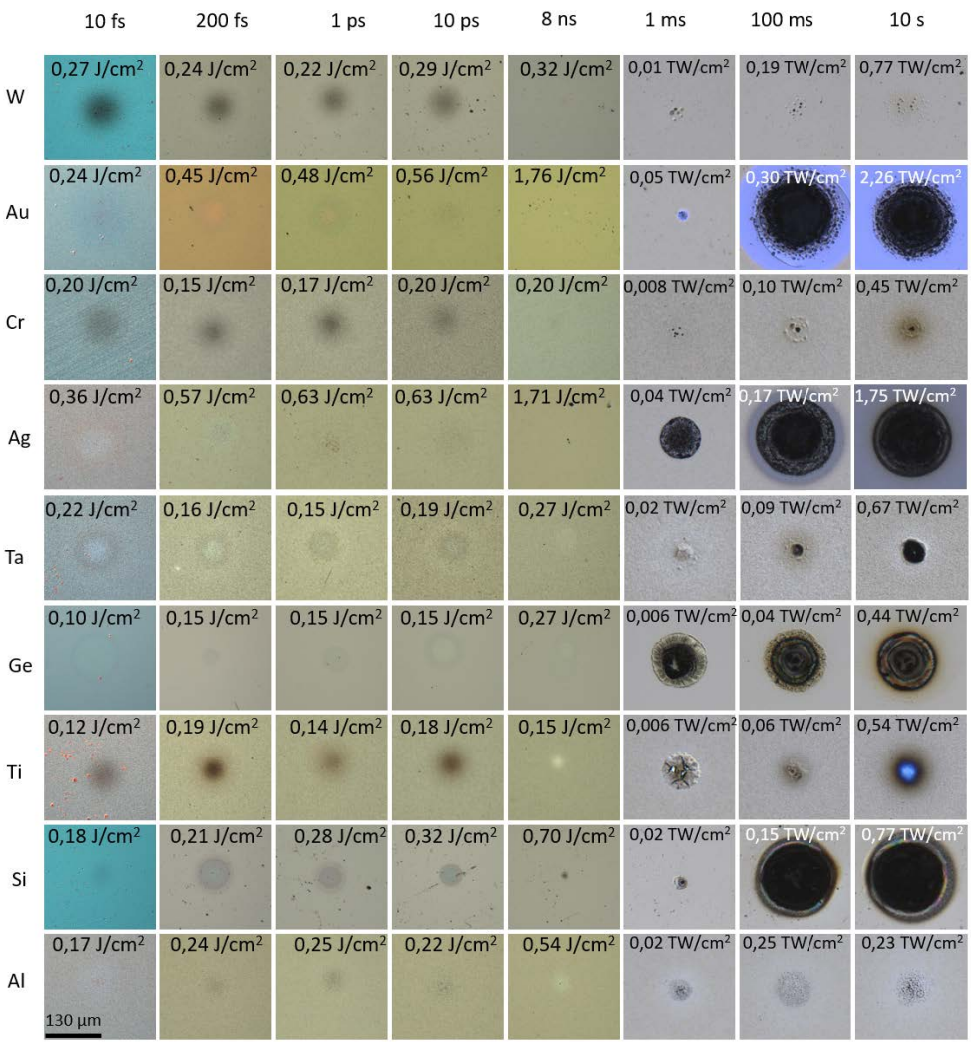

Fig. 3. 1-on-1 damage morphology.

Optics EXPRESS

for thermally-induced damage, various damage patterns are observed depending on the pulse duration and material properties.

For the shortest pulse durations, damage typically manifests as a heat-affected zone (HAZ) or a melting and re-solidification pattern, as observed in materials such as tungsten (W), chromium (Cr), and titanium (Ti). At intermediate pulse durations (200 fs – 8 ns), localized defect-driven damage becomes more prominent, often appearing as pinpoints, as is seen in silicon (Si), silver (Ag), and gold (Au). This suggests the presence of inhomogeneity, namely surface or thickness or substrate imperfections that locally heat up more rapidly than the surrounding material, leading to localized thermal stress and subsequent breakdown [37].

In the CW regime, higher-energy depositions are expected, and damage morphologies evolve further. We observe ablation craters and cracking, typically resulting from material melting and/or boiling, surrounded by pronounced HAZ. The typical morphology of CW-induced damage consists of a central region showing signs of boiling or melting, surrounded by ripple patterns and slip lines, most prominently seen in Ag, Au, and Ge coatings. These characteristics align well with previous observations of CW laser damage [12].

4.2. Experimental LIDT data and empirical scaling laws

This section presents experimental LIDT results in the range of 10 fs to 10 s at near-IR wavelengths (1030 nm, 1064 nm, 1070 nm) and discusses the empirical laws used to describe the tendencies. Figure 5 summarizes the LIDT data in all pulse durations and materials investigated for single-shot and multi-shot testing protocols.

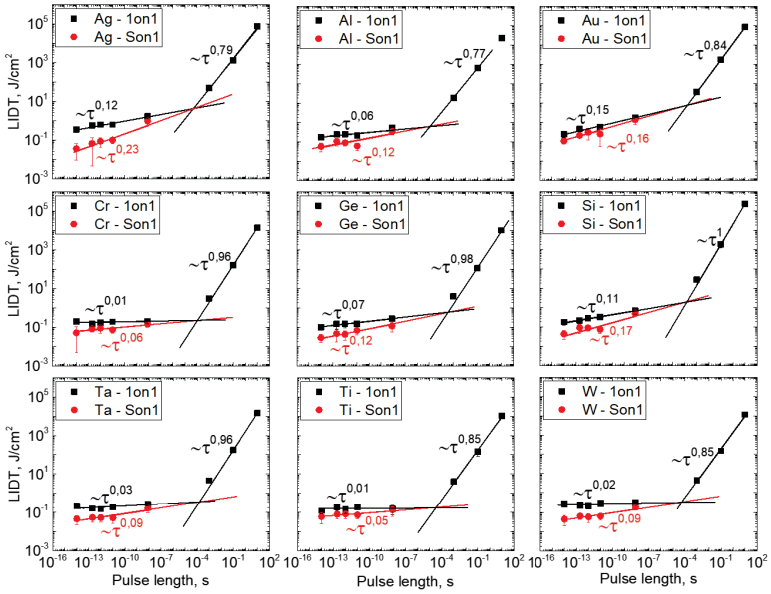

Fig. 4. Experimental data on 7 metallic and 2 semiconductor coatings with 1-on-1 and S-on-1 protocols. Solid lines represent empirical power-law fits. The cross-point between pulsed, and CW regimes indicates the thermal decay constant.

To evaluate the dependence of LIDT on pulse duration, we applied an empirical power-law approximation (LIDT $\sim \tau^x$). This scaling law was applicable in both pulsed and CW regimes:

- **Pulsed regime (10 fs < τ < 8 ns):** The dependence of LIDT on the duration of the pulse is weak, with empirical exponents ranging from 0.01 to 0.15 for damage thresholds of 1-on-1 and from 0.05 to 0.23 for S(1000)-on-1 thresholds (see Table 4), following

Optics EXPRESS

Eq. (4). The stronger dependence observed under multipulse conditions suggests that repeated exposure weakens the material, potentially altering its reflectivity due to surface modifications [10,12].

- **CW regime (1 ms < τ < 10 s):** In this regime, the dependence of LIDT on the duration of the pulse is nearly linear, with power-law exponents ranging from 0.77 to 1, consistent with Eq. (2).

Table 4. Empirical exponents (x) for power-law-based (LIDT ~ τ^x) scaling in pulsed and CW regimes, along with thermal decay constants.

	Exponent (1-on-1)		Exponent (S-on-1)	Thermal Decay Constant (ms)
Material	Pulsed	CW	Pulsed	τ_{TDC}
Ag	0.12	0.79	0.23	0.23
Al	0.06	0.77	0.12	0.01
Au	0.15	0.84	0.16	0.20
Cr	0.01	0.96	0.06	0.10
Ge	0.07	0.98	0.12	0.42
Si	0.11	1.00	0.17	0.13
Ta	0.03	0.96	0.09	0.17
Ti	0.01	0.85	0.05	0.09
W	0.02	0.85	0.09	0.19

The reduction in LIDT under multipulse exposure is attributed to the effects of material fatigue [10,38]. For metallic films, absorbed laser irradiation induces thermal expansion, which leads to strain in the near-surface region. If laser-induced stress exceeds the film strength, irreversible deformation occurs, increasing surface roughness and absorption [39]. Repeated thermal cycling can also cause micro-structural changes, contributing to optical failure [40], as well as surface oxidation at high temperatures, which can further modify absorption.

A critical feature in Fig. 3 is the transition point between the pulsed and CW regimes, corresponding to the thermal decay constant (TDC). It represents the characteristic time for the material to cool between pulses [8]. If the period between repetitive pulses is shorter than the TDC, heat accumulates over time, which may lead to delayed melting or thermal fatigue in the S-on-1 regime. For pulse durations longer than the TDC, heat dissipates efficiently during the pulse, reducing the sensitivity of LIDT to the pulse duration. Interestingly, both the 1-on-1 and the S(1000)-on-1 approximations converge at the same TDC, indicating that while fatigue influences the LIDT scaling, the TDC remains a fundamental material property.

To quantify the relationship between TDC and material parameters, we performed a polynomial regression analysis (see Fig. 5). The best-fit empirical model is:

$$\tau_{TDC} = 0.2353 - 3.269\times10^{-4}C + (C - 392.67)(h - 300.06)(-4.85\times10^{-7}) + 2.424\times10^{-4}h \quad (8)$$

where τ_{TDC} (ms) is the thermal decay constant, C (J/(kg · K)) is the specific heat capacity and h (nm) is the thickness of the material. This model suggests a complex dependence of τ_{TDC} on the heat capacity and coating thickness, with an interaction term $(C - 392.67)(h - 300.06)$ indicating a coupled effect between these properties.

4.3. Role of absorptance in LIDT

Following the predictions of Eqs. (2) and (4), LIDT should inversely correlate with the absorption of the material. To investigate this, we present experimental LIDT data for all coatings as a

Optics EXPRESS

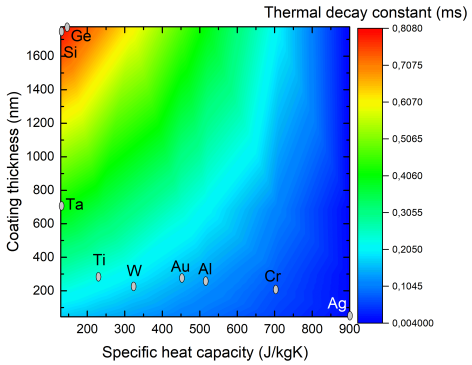

Fig. 5. 3D map showing the relationship between the thermal decay constant, coating thickness, and specific heat capacity.

function of inverse absorptance $(1/(1-R))$ for two pulse durations representing the pulsed and CW regimes (see Fig. 6: 10 ps for pulsed and 100 ms for CW), assuming negligible scattering losses. In the CW regime (100 ms, right Y-axis), a clear trend is observed: lower absorptance correlates with higher damage thresholds, which is consistent with theory and recent findings on hybrid metal-dielectric coatings under CW irradiation [41]. As expected, in the CW regime, the accumulation of heat in the substrate eventually leads to melting, following the predicted trend.

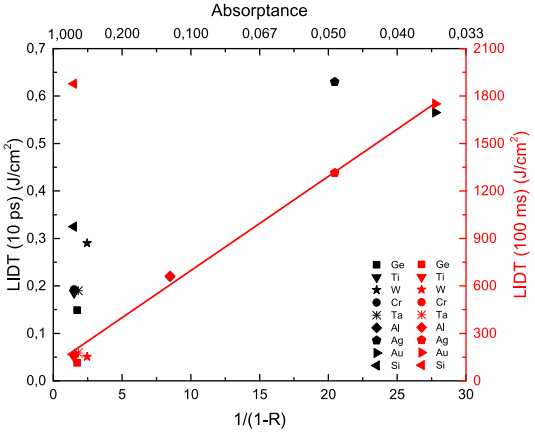

Fig. 6. LIDT as a function of inverse absorptance for 10 ps and 100 ms pulse durations for all coatings.

However, in the pulsed regime (10 ps, left Y axis), deviations arise primarily due to thermal capacity of the coating. For example, tungsten (W), with a high melting point (~3422°C), requires more energy to melt, leading to higher LIDT values. In contrast, silicon (Si) exhibits the highest resistance to laser damage when deposited on a transparent target. This is due to its partial transparency in the near-infrared range [42], which reduces energy absorption and thus increases LIDT.

4.4. Numerical LIDT Simulations of Gold and Silver Coatings

In Fig. 7(A), we directly compare the single shot experimental LIDT results for gold and silver coatings with first-order heat flow approximations (Eqs. (2) and (4), dashed curve) and numerical simulations using the Two-Temperature Model (solid curves). In the pulsed regime, there is

Optics EXPRESS

insufficient time for radial or longitudinal diffusion during the pulse. For longer pulses, heat loss to the substrate becomes significant, making the thermal properties of the substrate the dominant factor, as shown in Fig. 8. Thus, we used the material parameters of gold and silver for short pulses and the diffusion parameters of glass for CW. The first-order approximation predicts a transition from pulse width independence to a linear dependence on the pulse width. However, it lacks accuracy and fails to estimate LIDT correctly in absolute terms, as it neglects transient effects such as electron dynamics in the femtosecond regime, layer structure, and cylindrical geometry.

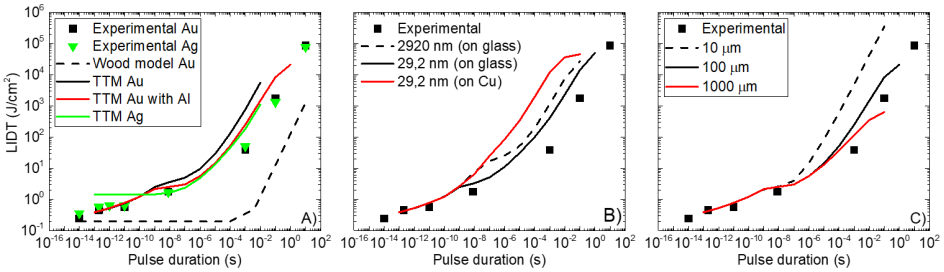

Fig. 7. A) LIDT simulations for gold and silver coatings using the model presented by Wood [8] and Two-Temperature Model, indicating the influence of adhesive layer within the coating stack. B) Effect of the gold layer on glass and copper substrates, C) effect of different beam diameters.

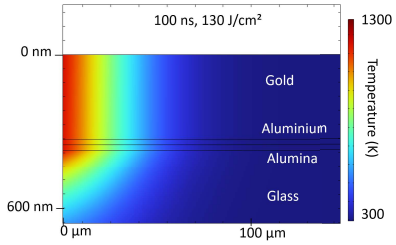

Fig. 8. Electron temperature distribution at the end of 100 ns laser pulse.

In contrast, the TTM closely matches the experimental gold data in the pulsed regime, with LIDT scaling as $\tau^{0.18}$ for short pulses (<10 ns). For long pulses (>100 ns), the LIDT scales as $\tau^{0.82}$, but the simulated values (black curve) were slightly higher than the experimental data. This discrepancy occurred because the melting point of the aluminum underlayer (660∘C) was not initially considered. After accounting for the aluminum underlayer melting point (red curve), the experimental data were better reproduced with TMM.

To assess the applicability of TTM, we also simulated use case of silver coating. In this case, the thickness of the Ag layer is comparable to the optical penetration depth, which limits the thermal diffusion along the depth of the layer. Consequently, a constant LIDT is expected across pulse durations. However, the TTM does not account for energy transport within the underlying Al buffer layer, introducing a limitation in the model. In reality, electronic heat diffusion within the Al layer may enhance energy dissipation, suggesting that the actual LIDT could be lower than predicted by the model.

We also investigated the LIDT scaling of the gold coating thickness. LIDT was calculated for two additional gold thicknesses (29.2 nm and 2920 nm), which are 10 times thinner and thicker than the nominal thickness (292 nm) of gold. In addition, we simulated the effect of the substrate by replacing glass with cooper (Cu), a material with one of the highest thermal conductivities.

Optics EXPRESS

As shown in Fig. 7(B), increased coating thickness and higher conductivity of Cu substrates lead to a higher LIDT for long pulses, as previously reported [14,15]. For short pulses, the thermal diffusion length is smaller than the film thickness, so heat dissipation remains confined within the metallic film, with the gold layer being the main factor. However, around 1 ns, the impact of the substrate on LIDT becomes significant. For pulses shorter than 1 ns, only the metallic layer is relevant.

Finally, we also simulated the effect of the diameter of the beam, revealing that the size of the beam alters the conditions of thermal radial diffusion, as noted in [8]. Simulations with 10 μm, 100 μm (nominal), and 1 mm diameters, shown in Fig. 7(C), confirm that threshold fluence depends on the beam size in the CW regime: smaller beams lead to higher radial heat losses and thus also higher LIDT.

5. Conclusions

In summary, we experimentally estimated LIDTs across pulse durations ranging from 10 fs to 10 s for various metallic and semiconductor coatings. The empirical LIDT scaling laws exhibit a power-law dependence on the duration of the pulse (LIDT $\sim \tau^x$) with distinct behaviors in the pulsed and continuous wave regimes. In the pulsed regime (10 fs – 9 ns), LIDT shows a weak dependence on the duration of the pulse (exponent x: 0.01 – 0.15 for 1-on-1; 0.05 – 0.23 for S(1000)-on-1), while in the CW regime (1 ms – 10 s), a nearly linear dependence is observed (exponent x: 0.77 – 1.00). The transition between these regimes is governed by the thermal decay constant, which is influenced by material properties such as specific heat capacity and coating thickness.

Our results also confirm that LIDT is inversely correlated with material absorptance. However, deviations in the pulsed regime imply additional influences from thermal capacity and melting temperatures, particularly for tungsten and silicon. Multi-pulse exposure in the pulsed regime indicates a mechanical fatigue effect, leading to an increased dependence of LIDT on pulse duration. The classical heat transport model successfully predicts the transition between pulsed and CW regimes; however, the Two-Temperature Model was necessary to achieve better agreement with the experimental data, strengthening the thermal model, presented by Wood, with essential adaptations for metallic coatings.

Both experimental and numerical LIDT results indicate that the thermal decay constant depends on the coating thickness and specific heat capacity, while simulations further highlight the role of substrate thermal diffusivity and beam diameter. Damage morphology analysis confirms that laser damage mechanisms are indeed primarily thermal. In the ultrashort-pulse regime, energy deposition can be precisely controlled, leading to heat-affected zones and melting patterns. For longer pulses, defect-driven damage and cracking occur because of localized heating, whereas CW irradiation results in extensive material modification, including ablation craters and ripple patterns.

Although the TTM can accurately simulate scaling laws, additional simulations are needed to enhance predictive models for laser damage resistance in optical coatings. Future work should focus on refining empirical scaling models for CW regimes and systematically investigating the combined effects of coating thickness, substrate properties, and beam diameter on LIDT, as well as addressing anomalies in scaling reported by other studies.

Funding. Lietuvos Mokslo Taryba (No. 01.2.2-LMT-K-718-01-0014, No. S-A-UEI-23-6); Laserlab-Europe (No. 871124); Deutsche Forschungsgemeinschaft (Project ID 448756425); Bundesministerium für Bildung und Forschung (13N1725); Bundesministerium für Bildung und Forschung (13F1000H).

Acknowledgments. The authors thank Algirdas Selskis (FTMC, Vilnius) for providing cross-sectional measurements of the coatings. The authors also thank Dr. Andreas Wienke from LZH (Germany) for discussions about the paper. This work has received funding from the European Union's Horizon 2020 research, and innovation program under (grant agreement No. 871124) Laserlab-Europe and European Regional Development Fund (project No. 01.2.2-LMT-K-718-01-0014) under a grant agreement with the Research Council of Lithuania (LMTLT) and "Universities'

Optics EXPRESS

Excellence Initiative" programme by the Ministry of Education, Science and Sports of the Republic of Lithuania under the agreement with the Research Council of Lithuania (project No. S-A-UEI-23-6). We also thank the BMBF for the funding of the projects "UV-Fatique" (13N17255) and "PriFUSIO" (13F1000H) and Deutsche Forschungsgemeinschaft (DFG) ("Fast Coatings," Project ID 448756425).

Disclosures. The authors declare no conflict of interest.

Data availability. Data underlying the results presented in this paper are not publicly available at this time but may be obtained from the authors upon reasonable request.

Supplemental document. See Supplement 1 for supporting content.

References

1. T. H. Maiman, R. H. Hoskins, I. J. D'Haenens, *et al.*, "Stimulated optical emission in fluorescent solids. ii. spectroscopy and stimulated emission in ruby," Phys. Rev. **123**(4), 1151–1157 (1961).
2. X. Yang, H. Xie, E. Alonas, *et al.*, "Mirror-enhanced super-resolution microscopy," Light: Sci. Appl. **5**(6), e16134 (2016).
3. T. Ştefanov, H. V. R. Maraka, P. Meagher, *et al.*, "Thin film metallic glass broad-spectrum mirror coatings for space telescope applications," J. Non-Crystalline Solids **7**, 100050 (2020).
4. T. Sandner, J. U. Schmidt, H. Schenk, *et al.*, "Highly reflective optical coatings for high-power applications of micro scanning mirrors in the UV-VIS-NIR spectral region," in *MOEMS Display, Imaging, and Miniaturized Microsystems IV*, vol. 6114 H. Ürey, D. L. Dickensheets, and B. P. Gogoi, eds., International Society for Optics and Photonics (SPIE, 2006), p. 61140H.
5. A. Piegari and F. Flory, "Optical Thin Films and Coatings: From Materials to Applications," Woodhead Publishing Series in Electronic and Optical Materials (Elsevier Science, 2018).
6. M. Sparks and E. Loh, "Temperature dependence of absorptance in laser damage of metallic mirrors: I. melting," J. Opt. Soc. Am. **69**(6), 847–858 (1979).
7. B. C. Stuart, M. D. Feit, S. Herman, *et al.*, "Optical ablation by high-power short-pulse lasers," J. Opt. Soc. Am. B **13**(2), 459–468 (1996).
8. R. M. Wood, *Laser-Induced Damage of Optical Materials* (CRC Press, 2003), 1st ed.
9. J. Pulsifer, M. Tillack, and S. Harilal, "Effect of laser pulse duration on damage to metal mirrors for laser ife," Proc. SPIE **6720**, 67200D (2007).
10. C. S. Lee, N. Koumvakalis, and M. Bass, "A theoretical model for multiple-pulse laser-induced damage to metal mirrors," J. Appl. Phys. **54**(10), 5727–5731 (1983).
11. N. Koumvakalis, C. S. Lee, and M. Bass, "Single And Multiple Pulse Catastrophic Damage In Diamond-Turned Cu And Ag Mirrors At 10.6, 1.06, And 0.532 mum," Opt. Eng. **22**(4), 419–423 (1983).
12. Y. Jee, M. F. Becker, and R. M. Walser, "Laser-induced damage on single-crystal metal surfaces," J. Opt. Soc. Am. B **5**(3), 648–659 (1988).
13. S. V. Starinskiy, Y. G. Shukhov, and A. V. Bulgakov, "Laser-induced damage thresholds of gold, silver and their alloys in air and water," Appl. Surf. Sci. **396**, 1765–1774 (2017).
14. G. Tsibidis, D. Mansour, and E. Stratakis, "Damage threshold evaluation of thin metallic films exposed to femtosecond laser pulses: The role of material thickness," Opt. Laser Technol. **156**, 108484 (2022).
15. M. Domke, L. Nobile, S. Rapp, *et al.*, "Understanding thin film laser ablation: The role of the effective penetration depth and the film thickness," Phys. Procedia **56**, 1007–1014 (2014). 8th International Conference on Laser Assisted Net Shape Engineering LANE 2014.
16. Z. Li, E. Palacios, S. Butun, *et al.*, "Omnidirectional, broadband light absorption using large-area, ultrathin lossy metallic film coatings," Sci. Rep. **5**(1), 15137 (2015).
17. M. Trubetskov, T. Amotchkina, L. Lehnert, *et al.*, "Broadband phase-shifting mirrors for ultrafast lasers," Appl. Opt. **59**(5), A123–A127 (2020).
18. G. Wang, T. Liu, J. Chao, *et al.*, "Recent advances and challenges in ultrafast photonics enabled by metal nanomaterials," Adv. Opt. Mater. **10**(11), 2200443 (2022).
19. N. Zheng, R. Buividas, H.-h. Huang, *et al.*, "Laser machining at high pw/cm2 intensity and high throughput," Photonics **11**(7), 598 (2024).
20. S. Butkus, V. Jukna, E. Kazukauskass, *et al.*, "High-contrast marking of stainless-steel using bursts of femtosecond laser pulses," Micromachines **14**(1), 194 (2023).
21. B. Neuenschwander, B. Jaeggi, M. Schmid, *et al.*, "Optimization of the volume ablation rate for metals at different laser pulse-durations from ps to fs," in *Laser Applications in Microelectronic and Optoelectronic Manufacturing (LAMOM) XVII*, vol. 8243 G. Hennig, X. Xu, B. Gu, and Y. Nakata, eds., International Society for Optics and Photonics (SPIE, 2012), p. 824307.
22. T. Genieys, M. Sentis, and O. Utéza, "Measurement of ultrashort laser ablation of four metals (al, cu, ni, w) in the single-pulse regime," Adv. Opt. Technol. **9**(3), 131–143 (2020).
23. J. Yang, Y. Zhao, N. Zhang, *et al.*, "Ablation of metallic targets by high-intensity ultrashort laser pulses," Phys. Rev. B **76**(16), 165430 (2007).
24. N. Hodgson, S. Heming, A. Steinkopff, *et al.*, "Lasers in manufacturing conference 2019 ultrafast laser ablation at 1035 nm, 517 nm and 345 nm as a function of pulse duration and fluence," (2019).

Optics EXPRESS

25. M. Hashida, A. Semerok, O. Gobert, *et al.*, "Ablation threshold dependence on pulse duration for copper," Appl. Surf. Sci. **197-198**, 862–867 (2002). COLA'01 SI.
26. Y. Zhu, Y. Ma, W. Cheng, *et al.*, "Laser-induced damage thresholds in sio2-coated aluminum mirrors under various ultrashort pulse widths," Appl. Opt. **64**(5), 1235–1245 (2025).
27. "Lasers and laser-related equipment — test methods for laser-induced damage threshold — part 2: Threshold determination," Standard 21254-2:2011(en), International Organization for Standardization (2011).
28. P. Tipler, *Physics for Scientists and Engineers: Vol. 1: Mechanics, Oscillations and Waves, Thermodynamics, Physics for Scientists and Engineers* (W. H. Freeman, 1999).
29. J. Ma and C. Zhang, "Ignition thresholds and flame propagation of methane/air mixtures ignited via radiatively heated inert particles," Energies **14**(16), 5173 (2021).
30. D. Strickland and G. Mourou, "Compression of amplified chirped optical pulses," Opt. Commun. **55**(6), 447–449 (1985).
31. A. Dubietis, G. Jonušauskas, and A. Piskarskas, "Powerful femtosecond pulse generation by chirped and stretched pulse parametric amplification in bbo crystal," Opt. Commun. **88**(4-6), 437–440 (1992).
32. R. Budriūnas, T. Stanislauskas, J. Adamonis, *et al.*, "53 w average power cep-stabilized opcpa system delivering 5.5 tw few cycle pulses at 1 khz repetition rate," Opt. Express **25**(5), 5797–5806 (2017).
33. X. Y. Wang, D. M. Riffe, Y.-S. Lee, *et al.*, "Time-resolved electron-temperature measurement in a highly excited gold target using femtosecond thermionic emission," Phys. Rev. B **50**(11), 8016–8019 (1994).
34. Z. Lin, L. V. Zhigilei, and V. Celli, "Electron-phonon coupling and electron heat capacity of metals under conditions of strong electron-phonon nonequilibrium," Phys. Rev. B **77**(7), 075133 (2008).
35. B. Wang and L. Gallais, "A theoretical investigation of the laser damage threshold of metal multi-dielectric mirrors for high power ultrashort applications," Opt. Express **21**(12), 14698–14711 (2013).
36. S. I. Anisimov and B. S. Luk'yanchuk, "Selected problems of laser ablation theory," Phys.-Usp. **45**(3), 293–324 (2002).
37. D. Ristau, *Laser-induced damage in optical materials* (CRC Press, 2014).
38. H. M. Musal, "Thermomechanical stress degradation of metal mirror surfaces under pulsed-laser irradiation," Laser Induced Damage in Optical Materials: 1979 pp. 159–173 (1980).
39. A. Rosenfeld, M. Lorenz, R. Stoian, *et al.*, "Ultrashort-laser-pulse damage threshold of transparent materials and the role of incubation," Appl. Phys. A **69**(7), S373–S376 (1999).
40. C. Meng, C. Wu, X. Wang, *et al.*, "Effect of thermal fatigue on microstructure and mechanical properties of h13 tool steel processed by selective laser surface melting," Metals **9**(7), 773 (2019).
41. K. Kiedrowski, M. Jupé, H. Ehlers, *et al.*, "Challenges in the development of a reliable cw-lidt measurement routine," Opt. Mater. Express **13**(6), 1712–1725 (2023).
42. D. Franta, D. Necas, L. Zajíčková, *et al.*, "Advanced modeling for optical characterization of amorphous hydrogenated silicon films," Thin Solid Films **541**, 12–16 (2013).